KOM
CORROSION AND MATERIAL PROTECTION JOURNAL

ORIGINAL ARTICLE

sciendo

Influence of temperature and thermal cycles on the corrosion mechanism of wrought AZ91D magnesium alloy in simulated sea water solution

Hariesh S.P.[1], Dhanyanth P.V.[1], Kughan S.A.[1], Dhanush K. Babu[1], Vaira Vignesh R.[1], Sathiya P.[2]
[1] Department of Mechanical Engineering, Amrita School of Engineering, Coimbatore, Amrita Vishwa Vidyapeetham, India
[2] Department of Production Engineering, National Institute of Technology, Tiruchirappalli, India
E-mail: r.vairavignesh@gmail.com, r_vairavignesh@cb.amrita.edu

This study successfully conducted a comprehensive analysis of the AZ91D magnesium alloy, encompassing microstructural, mechanical, and corrosion assessments. The microstructure consisted of primary α-Mg crystals and an aluminum-rich α-Mg/β-Mg17Al12 eutectic phase, with intermetallic phases predominantly precipitating at grain boundaries. The microhardness was quantified at 49.96 ± 1.76 HV. Thermostatic tests unveiled a noTab. increase in corrosion rates with rising temperatures, signaling reduced corrosion resistance at elevated environments. Conversely, thermos-cyclic tests showed relatively lower corrosion rates attributed to the accumulation of protective debris on the specimen surface, which could mitigate corrosion during temperature fluctuations. Electrochemical corrosion behavior revealed susceptibility to pitting corrosion at –1.204 V, limiting its application as a sacrificial anode in marine settings.

INTRODUCTION

Corrosion in ship hulls is one of the greatest threats to the aesthetics and safety of critical types of machinery [1-4]. Iron alloys are typically used in the ship, constituting the main body to the smallest element onboard. The outer body of the ship, which is in contact with the seawater, is more prone to corrosion. The attribuTab. factors to corrosion include the chemical activity of iron alloys and the high reactivity of chloride ions [5-7]. Also, the difference in the corrosion potential of iron alloys (structural members) and copper alloys (turbine blades) induces electrochemical corrosion. The losses resulting from corrosion in the marine industry during construction and operation amount to around 50-80 billion USD and 3% of global GDP. Statistics indicate that 90% of ship breakdowns are caused by corrosion.

Industrial practices for reducing the effects of corrosion include painting, anti-corrosion coatings, and cathodic protection through sacrificial anodes or impressed current methods [8-10]. The sacrificial anodes provide effective corrosion protection to marine structures. The sacrificial anodes divert corrosive processes away from critical components by serving as sacrificial electrodes. The sacrificial anodes operate independently of any external power source. Also, the sacrificial anodes are simple to install and much easier to inspect. The commonly used sacrificial anode materials include highly active metals such as magnesium (Mg), aluminum (Al), and zinc (Zn) [11, 12].

Magnesium is the lightweight metal [13-15] and has the highest driving voltage (−2.373 V_{SHE}) of any material utilized to create sacrificial anodes [16-22]. However, the corrosion rate of magnesium varies between 4 and 8 mm/year in marine environments [23-26]. Hence, the corrosion mandates frequent replacement of magnesium anodes. This highlights the need to improve the life of anodes without compromising the anodic efficiency.

Loto et al. [27] studied the anodic behavior of galvanized magnesium anode for cathodic protection of mild steel in seawater and 0.5M H_2SO_4 with different cross-sectional areas. The anode size was inversely proportional to the corrosion rate of mild steel in seawater and H_2SO_4. For an increase of 50 mm^2 area, the corrosion rate was decreased from 0.062-0.007 mm^2/yr, which was 88.71% efficient. Azzeddine et al. [28] studied the corrosion behavior of binary magnesium-rare earth alloys through electrochemical tests in a 3.5% wt NaCl solution. Mg-0.41Dy alloy had the highest corrosion resistance of 5.58 Ω.cm^2, as the Dy_2O_3 layer formed prevented pitting corrosion. However, Mg-1.43La alloy exhibited severe pitting corrosion and had a low corrosion resistance of 2.89 Ω.cm^2.

May et al. [29] assessed the performance of magnesium anodes manufactured under the sintering process. Corrosion potential and electrochemical impedance spectroscopy tests were carried out to test the anodic behavior of Mg, Mg-1Nb, and Mg-1Cr anodes. Mg-Nb/X52 system

had a better result because the current drained by the system was constant (480 mA/m^2) with a potential of –1.2 V throughout the experiment. Zidane et al. [30] eva-luated the corrosion of AZ31Mg alloy as a sacrificial anode for protecting a tank that had hot water with chlorine. The alloy was immersed in an aqueous NaCl solution of various concentrations at 20 °C to ascertain its chemical behavior in environments simulated drinking. The formation of $Mg(OH)_2$ reduced the corrosion rate of the tank from 46.1 to 13.3 mm/year over 48 hours of immersion.

Rzychon et al. [31] evaluated the corrosion resistance of Mg-RE-Zr alloys (WE43, WE54, and Elektron 21). The immersion test was carried out for 7 days in 3.5% NaCl solution. WE43 (0.26 mg/cm^{2}day) had the least corrosion rate, whereas WE54 (0.62 mg/cm^2 day) and Elektron 21 (1.43 mg/cm^2 day) had more corrosion rate. Elektron 21 had pitting corrosion, and the other alloys had intergranular corrosion. Hence, the grain boundaries of alloys influenced the initiation of corrosion sites. Yasakau et al. [32] analyzed the anodic sacrificial protection of Mg5Gd alloy coated with Mg5Gd through magnetron sputtering. An immersion test in Hank's balanced salt solution (HBSS) was performed. The coated specimen (>0.5 mm/year) resulted in better corrosion resistance than the uncoated ones (5 mm/year)

Umoru et al. [33] investigated the effect of tin in Al–Zn–Mg alloy as a sacrificial anode in seawater. The alloy with 0%, 0.01%, 0.05% and 0.1% Sn were tested. The anodic efficiency increased with an increase in Sn. After 336 hours of being immersed in seawater, the alloy with 0.1% Sn exhibited 99.53% efficiency, whereas the alloy with 0% Sn exhibited 98.32% efficiency. Quevedo et al. [34] studied the effect of turbulent flow on the corrosion of Al–Zn–Mg alloy in artificial seawater media in a rotating cylinder setup. The corrosion, controlled by charge transfer kinetics, increased with the rotation rate. The availability of oxygen on the surface was attributed to the high corrosion rate of the specimens. The charge transfer resistance under turbulent conditions decreased significantly to 99.39, 70.67, 67.15, and 59.7 $\Omega \cdot cm^2$ for the different rotation rates 1000, 3000, 5000, and 7000 rpm, respectively.

The results of extensive laboratory anode efficiency investigations and field tests of Robison et al. [35] revealed that 6% Al-3% Zn magnesium alloy cast anodes need low impurity levels. Laboratory testing admitted that the impurities (nickel, copper, and silicon) decreased the efficiency of Mg alloy. Superior performance was provided by the practicable casting composition of low iron (0.003%) with moderate Mn (<0.15%) concentration. Sun et al. [36] evaluated the corrosion behavior and working performance of Al–Zn–In–Mg–Ti in deep waters as a sacrificial anode through potentiodynamic polarization, self-discharge, and electrochemical impedance spectroscopy. The system's current efficiency of the sacrificial anodes was about 70-80 %. The average corrosion rate was 1.6438 ±0.2905 ×10^{-6} g.cm^{-2} in simulated deep waters.

Muazu et al. [37] fabricated an Al–Zn–Mg sacrificial anode from recycled aluminum and zinc. Characterization results revealed that $MgZn_2$ phases were responsible for the pitting corrosion. However, heat treatment coarsened the sTab. $MgZn_2$ phase particles in the Al matrix. The microstructure lowered the corrosion resistance of the alloy, and that, in turn, improved anode efficiency. Pathak et al. [38] described that cathodic protection technology aims to utilize a structural metal surface as the cathode of a galvanic cell to generate an electrical circuit to control corrosion. The corrosion rate of Mg alloys was fairly low at pH between 4 and 14. Small amounts of cerium oxide applied to a Mg-rich primer significantly increased the resistance of AZ91D magnesium alloy.

Sekar et al. [39] investigated the effect of equal channel angular pressing on galvanic corrosion of ZE41 alloy against AA7075 alloy using EIS measurements and potentiodynamic polarization. The galvanic corrosion resistance was (0.05 mm/year) 58% and (11.171 mm/year) 54% with 0 and 1M NaCl respectively. Kajánek et al. [40] experimented on corrosion degradation of plasma electrolytic oxidation coated AZ31 Mg alloy. The corrosion mechanism was evaluated after 24 hours of salt spray testing. The polarization resistance of PEO coated specimen was 18399 $\Omega.cm^2$. The results indicated that the corrosion products covered scratches of PEO coating, reducing the anodic reaction.

Muazu et al. [41] researched variations in sacrificial anode stability and polarization potential in Al–*x*Zn–*x*Mg alloy in seawater. The alloy was connected to a digital multimeter to measure polarization potential. The sacrificial anode degree of protection for Al–8%Zn–4%Mg was higher (96.69) during the eighth week of exposure to seawater. Radhika et al. [42] experimented on stress corrosion resistance of friction stir processed and micro-arc oxidation coated ZE41 alloy. The threshold stress of SCC for BM was 25.8 MPa, FSP ZE41 was 60 MPa, MAO ZE41 was 30 MPa, and FSP-MAO ZE41 was 120 MPa. The MAO layer delayed the SCC crack propagation in the initial stages of corrosion.

In this study, AZ91D alloy was comprehensively assessed for microstructure, microhardness, corrosion characteristics, and sacrificial anodic performance. AZ91D alloy was exposed to thermal cycles involving static and dynamic temperature variations. Subsequently, potentiodynamic and galvanostatic tests were conducted to assess its electrochemical characteristics (corrosion and anodic performance). The findings were substantiated using advanced instrumental characterization to determine the effectiveness of AZ91D alloy as a sacrificial anode in marine environments.

Tab. 1. Composition of AZ91D alloy

Element	Mg	Al	Zn	Mn	Fe	Cu	Ni	Si
Composition (weight %)	90.4	8.72	0.51	0.31	0.001	0.002	0.001	0.04

MATERIALS AND METHODS

Materials

Commercially available AZ91D alloy, obtained from NextGen Steels and Alloys in India, was utilized as the base material for the study. The alloy, in its wrought form, had a thickness of 4 mm. The composition of the as-received AZ91D alloy is shown in Tab. 1, which was provided by Perfect Test Services, Coimbatore.

Microstructure

A specimen of dimension 10 mm × 10 mm × 5 mm was cut from the AZ91D alloy and cold-mounted using the standard polymeric compound. The specimen was polished per the metallographic specimen preparation guidelines of the standard ASTM E3-11 utilizing a bench grinder, emery sheets, and disc polishing units. Acetic picral etchant was prepared by mixing 5 ml acetic acid, 6 g picric acid,10 ml distilled water, and 100 ml ethanol. The specimen was immersed in the etchant for 15 seconds. Then, the specimen was rinsed in acetone and air-dried. The etched specimen was examined in an optical microscope (Carl Zeiss; Axiovert 25).

Microhardness

A specimen of dimension 10 × 10 × 5 mm was cut from the AZ91D alloy and polished per the standard metallographic preparation guidelines. The microhardness was measured using a Vicker's microhardness tester (Mitutoyo; MVK-H11). The microhardness tester utilized a diamond indenter to indent the specimen under an axial load of 300 gf for 15 seconds.

Immersion corrosion test

Thermo-static corrosion test

Specimens of dimension 10 × 10 × 5 mm were cut from the AZ91D alloy and polished in line with the standard ASTM E3-11. The polished specimens were degreased with acetone. The dimensions of the specimens were measured using a digital vernier caliper with a least count of 0.01 mm. The mass of the specimens was measured using a precision weighing balance with a readability of 0.0001 g. Then, the specimens were positioned in the conical flask (resting on the edges and slanting against the wall of the conical flask). The simulated seawater solution was prepared by mixing 3.5 g NaCl in 100 ml of distilled water. The simulated seawater solution was siphoned to a conical flask by maintaining a constant volume to exposed surface area ratio. The conical flask was closed using a stopper and placed in the corrosion test chamber (CM Envirosystems; NBT-80-A-1K-EP). The specimen was subjected to thermo-static corrosion at room temperature (27 °C), 20 °C, 40 °C, 60 °C, and 80 °C for 8 hours. After the test duration, the specimens were removed from the flask and air-dried. The adherent corrosion products were cleaned using boiling chromic acid solution (15 g of CrO_3 in 100 ml of distilled water) for 1 minute and rinsed in acetone. The mass of the corroded and cleaned specimens was measured using the precision weighing balance. The specimen code and testing conditions are shown in Tab. 2.

Tab. 2. Specimen code for thermos-static corrosion test

Sl.	Specimen code	Testing condition	Corrosion rate
1.	BM-RT-8	27°C for 8 hours	6.35 mm/year
2.	BM-RT-24	27°C for 24 hours	10.88 mm/year
3.	BM-20-8	20°C for 8 hours	4.63 mm/year
4.	BM-40-8	40°C for 8 hours	6.99 mm/year
5.	BM-60-8	60°C for 8 hours	8.22 mm/year
6.	BM-80-8	80°C for 8 hours	14.00 mm/year

Thermo-cyclic corrosion test

Specimens measuring 10 × 10 × 5 mm were cut from the AZ91D alloy and underwent standard ASTM E3-11 polishing. Subsequently, the polished samples were cleaned with acetone to remove the contaminants. The sample dimensions were determined using a digital vernier caliper with a precision of 0.01 mm. At the same time, their mass was assessed with a high-precision weighing balance with a readability of 0.0001 g. The specimens were carefully positioned within a conical flask, resting on their edges and leaning against the inner wall of the flask. 3.5 g NaCl was mixed with 100 ml of distilled water to create a simulated seawater solution. The solution was then transferred to the conical flask, maintaining a consistent ratio of volume to exposed surface area. The conical flask was closed using a stopper and placed in the corrosion test chamber (CM Envirosystems; NBT-80--A-1K-EP). The specimen underwent a corrosion test involving continuous exposure to temperatures of 20 °C, 40 °C, 60 °C, and 80 °C for 8 hours each, sequentially. The entire testing cycle was repeated five times, resulting in a total test duration of 360 hours. After the test duration,

the specimens were removed from the flask and air-dried. The adherent corrosion products were cleaned using boiling chromic acid solution (15 g of CrO_3 in 100 ml of distilled water) for 1 minute and rinsed in acetone. The mass of the corroded and cleaned specimens (BM-CYC-360) was measured using the precision weighing balance. The corrosion rate was evaluated using equation (1).

$$\text{Corrosion rate} = \frac{8760 \times \text{Mass Loss}}{\text{Density} \times \text{Surface area} \times \text{Time}} \quad (1)$$

Electrochemical corrosion

The electrolyte (simulated seawater solution) was prepared by adding 3.5% NaCl in 100 ml of distilled water. The specimen, with a dimension of 10 × 50 mm, was cut from AZ91 alloy. The specimens were polished as per the standard metallographic polishing guidelines utilizing a bench grinder, emery sheets, and disc polishing units. The polished specimen was wiped with ethanol and dried in hot air. The masking was wound on the specimen such that only 0.5 mm^2 area was exposed to the simulated seawater solution. An electrochemical workstation (CH Instruments; CHI604E) was used to analyze the electrochemical characteristics of the specimens. The electrochemical cell setup was established using a reference electrode (Ag/AgCl electrode), counter electrode (Pt wire), and the working electrode (polished specimen). The electrochemical cell setup was positioned inside the cylindrical beaker containing a simulated seawater solution. The distance between the reference electrode and working electrode was minimized through a luggin capillary tube. The open circuit potential (OCP) was initially established for the working electrode for 480 min. The open circuit potential was considered as the reference potential for the potentiodynamic polarization test. The potentiodynamic polarization test was performed by polarizing the specimen cathodically/anodically with respect to the OCP. The Tafel region was obtained through the plot (log I vs. V), which was utilized to extrapolate the Tafel parameters, corrosion current, and corrosion potential.

Sacrificial anodic performance

The sacrificial anodic performance test was performed per the DNV-RP-B401 standard. Specimens, sized 50 × 10 × 5 mm, were cut from the workpiece. The polished side of the working electrode specimen was covered with insulation tape, exposing only 1 mm^2. The counter electrode was a 40 × 10 × 5 mm SS316LN specimen, with an exposed area of 20 mm^2 left after masking with insulation tape. A reference electrode, Ag/AgCl, was used. The mass of the specimens was measured with a precision balance accurate to 0.0001 g. An artificial seawater electrolyte solution was prepared as previously described. The galvanostatic test was carried out at room temperature using a custom sacrificial anode test rig (CH Instruments). The anodic current density was held at 15 $\mu A.cm^{-2}$, 4 $\mu A.cm^{-2}$, 40 $\mu A.cm^{-2}$, and 15 $\mu A.cm^{-2}$ for an hour. The potential, time, and mass loss of the specimens were recorded to determine electrochemical efficiency and anode consumption rate.

$$\text{Electrochem. efficiency} = \frac{\text{Total current} \times \text{Time}}{\text{Mass loss}} \text{ (Ah/kg)} \quad (2)$$

$$\text{Anode consumption rate} = \frac{\text{Mass loss}}{\text{Total current} \times \text{Time}} \text{ (kg/Ah)} \quad (3)$$

$$\text{Anodic efficiency (\%)} = \frac{\text{Calculated current capacity}}{\text{Theoretical current capacity}} \times 100 \quad (4)$$

Advanced instrumental characterization

Field Emission Scanning Electron Microscopy (SEM; Zeiss Sigma; Gemini 300) was used to analyze the microstructure and corroded surface morphology of the corroded specimens. Energy dispersive X-ray spectroscopy (EDS) was used to determine the elemental composition and elemental map of the corrosion products and corroded areas in the specimens at a high electron tension of 20 kV.

RESULTS AND DISCUSSIONS

Microstructure and microhardness

The microstructure obtained for the specimen BM is depicted in Fig. 1a,b. The BM displayed a non-equilibrium dendritic microstructure comprising primary α-Mg (white phase) and an eutectic phase [43, 44]. The eutectic consisted of a secondary aluminum-rich α-Mg phase and an intermetallic β-$Mg_{17}Al_{12}$ phase (dark phase). Intermetallic phases precipitated in various shapes at grain boundaries. The microhardness for the specimen tested is 49.96 ±1.76 HV.

Immersion corrosion test

Thermo-static testing

During the comprehensive examination at different temperatures ranging from 20 °C to 80 °C, precise corrosion rates were meticulously recorded for the thermostatic test in 3.5% NaCl solution. The corrosion rate of the specimens is given in Tab. 2. At room temperature (27 °C), the corrosion rate was calculated to be 6.35 mm/ /year. The corrosion rates at these distinct temperature points were as follows: at 20 °C, the rate measured 4.63 mm/year, which increased to 6.99 mm/year at 40 °C, further elevated to 8.22 mm/year at 60 °C and dramatically spiked to 14.00 mm/year at 80 °C.

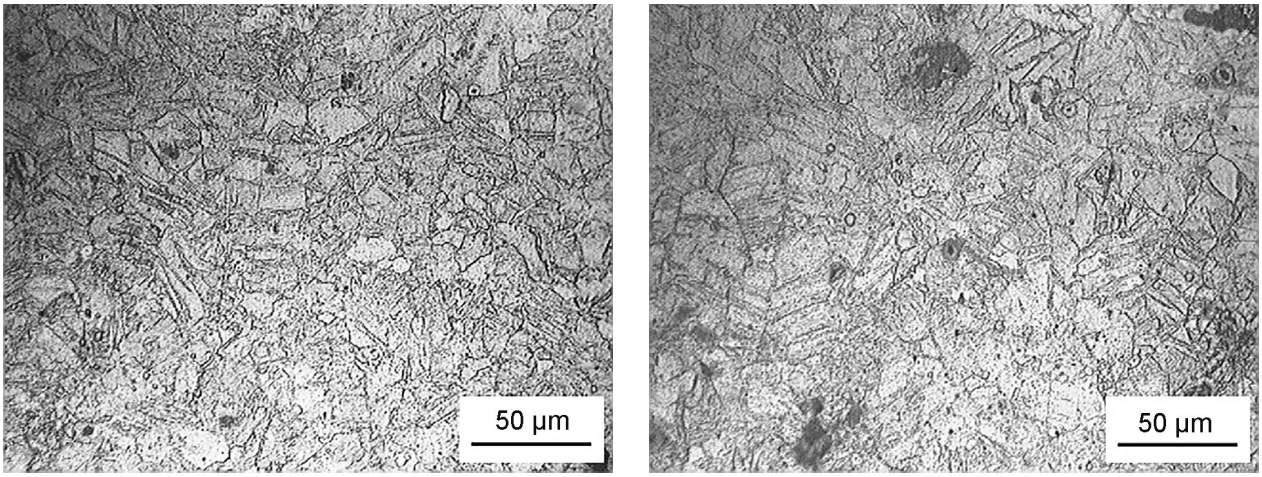

a) b)

Fig. 1. Microstructure of the specimen

At 40 °C, the specimen had a 10.14% surge in the corrosion rate compared to the rate observed at 20 °C. As the temperature continued to rise to 60 °C, the corrosion rate displayed a more pronounced acceleration, surging by 29.5% relative to the 20 °C baseline. However, the most dramatic transformation occurred at a scorching 80°C, where the corrosion rate rose steeply by 120.472% when contrasted with the reference point at 20 °C.

Fig. 2a shows the surface morphology with cracks and corrosion debris on the surface of the specimen BM-RT-8. The hydroxide ions in the electrolyte reacted with magnesium to form magnesium hydroxide, as given by equation (5). The volume of magnesium hydroxide exceeded that of magnesium, leading to the expansion of the surface layer. The surpassed surface layer expansion crossed the critical strength limit and was ultimately

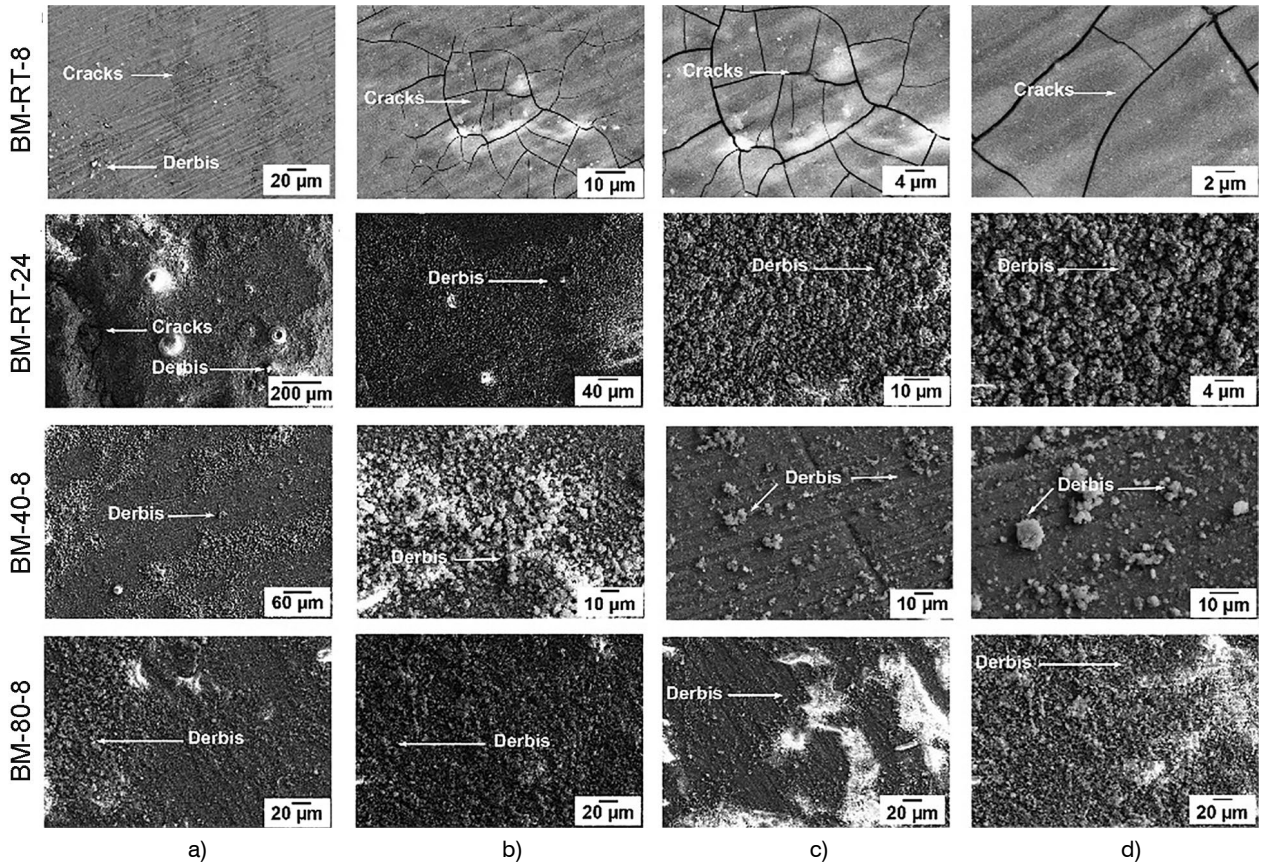

a) b) c) d)

Fig. 2. Surface morphology of specimens subjected to thermos-static test

fractured. The cracks exhibited an average width of 0.5 μm. Also, some corrosion debris was observed on the surface.

$$Mg^{2+} + 2OH^- \rightarrow Mg(OH)_2 \quad (5)$$

Fig. 2b shows the surface morphology of the specimen BM-RT-24. The subsequent reaction of magnesium hydroxide with chloride created corrosion debris. The corrosion debris particles collectively possessed an average diameter of 2 microns. Also, cracks and a large fraction of corrosion debris were observed on the surface. The debris formation was higher than BM-RT-8, which could be attributed to the increased immersion period. Also, the cracks were wider, with an average width of 10 μm than the specimen BM-RT-8. Fig. 2c shows the surface morphology of the specimen BM-40-8 with corrosion debris scattered on the surface. Compared to BM-RT-8, the debris deposition was higher, which is attributable. to the increase in the corrosion rate. Fig. 2d shows the large fraction of corrosion debris on the surface of the specimen BM-80-8. Compared to the other specimens, BM-80-8 had the highest debris depositions.

The elemental composition of the specimens is given in Tab. 3. BM-RT-24. BM-RT-24 contained a significant amount of magnesium at 58.88 wt.% and oxygen at 38.68%, suggesting a substantial formation of hydroxide compound on the surface. Sodium and chlorine concentrations were notable at 1.04 wt.% and 1.28 wt.%, indicating a degree of corrosion. Similarly, specimen BM-40-8 and specimen BM-80-8 exhibited relatively similar compositions. BM-40-8 was characterized by magnesium at 69.16 wt.%, oxygen at 29.45 wt.%, sodium at 0.45 wt.%, and chlorine at 0.76 wt.%. The specimen BM-80-8 possessed magnesium at 46.13 wt.%, oxygen at 50.30 wt.%, sodium at 1.50 wt.%, and chlorine at 1.24%. The higher oxygen concentration substantially formed a hydroxide compound on the surface, similar to specimen BM-RT-24. The elemental map of the corroded region of specimen BM-RT-24 and specimen BM-80-8 is shown in Fig. 4a,b. The major area in the individual elemental map of Mg and Cl superimposed with each other than Na and Cl. Hence, the composition map confirmed that the corrosion debris predominantly contained $MgCl_2$. This, in turn, indicated that NaCl was not precipitated on the surface during the immersion period. Also, the predominance of oxygen indicated the formation of $Mg(OH)_2$ on the surface.

The typical surface morphology of the specimen (BM-20-8) after removing the corrosion products is Fig. 3a. Pits, characterized by small concealed cavities or pits, and craters were observed on the surface. Pits were formed because of intense localized anodic reactions resulting from a greater electron demand originating from a larger cathodic area. The process ultimately leads to significant deterioration beneath a thin surface layer of oxide layer. The pits had an average diameter of ~7 μm. However, the depth of pits differed in each zone. Fig. 3b shows the surface morphology of the specimen BM-60-8 that established severe pitting corrosion. Also, the average size of the pits was ~15 μm.

The typical elemental composition of specimen BM-20-8 and specimen BM-60-8 after removal of corrosion products is given in Tab. 3. Both the specimens had a predominant concentration of magnesium (>90 wt.%) supplemented by small amounts of aluminum and zinc. Sodium and chlorine were present in trace amounts, and oxygen concentration was relatively lesser. The findings confirmed the effectiveness of boiling chromic acid solution in removing the adherent corrosion products from the surface. The elemental map of specimen BM-20-8 and specimen BM-60-8 after removal of corrosion products is shown in Fig. 5a,b. The cleaned surface was devoid of any corrosion products, as evidenced by the individual elemental maps of sodium, aluminum, and zinc.

Alloy composition (aluminum, zinc, and manganese) plays an integral role in the corrosion behavior of AZ91D alloy in marine environments. Crucially, AZ91D alloy is supposed to have superior corrosion resistance because of its higher aluminum content. The advantage stems from aluminum forming a protective oxide layer on the surface, acting as a robust barrier against further corrosion. However, electrochemical reactions underpin the corrosion process in seawater. For magnesium alloys, two pivotal reactions include the anodic reaction, where magnesium undergoes oxidation to form magnesium ions (equation (6)), and the cathodic reaction, which involves the reduction of water into hydrogen gas and hydroxide ions (equation (7)) [45].

$$Mg \rightarrow Mg^{2+} + 2e^- \quad (6)$$

$$2H_2O + 2e^- \rightarrow H_2 + 2OH^- \quad (7)$$

The reactions showcase the intricate interplay between magnesium and seawater, where magnesium ions are produced while water molecules are simultaneously reduced, culminating in the formation of corrosion products. The formation of a protective oxide layer stood as a basis for the corrosion resistance of magnesium alloy in seawater. The protective layer primarily consisted of magnesium hydroxide ($Mg(OH)_2$). Additionally, the presence of aluminum in the alloy contributed to forming

Tab. 3. The elemental composition of the corroded specimens

Sl.	Specimen	Elemental Concentration (wt. %)					
		Mg	Al	Zn	Na	Cl	O
1	BM-RT-24	58.88	0.02	0.10	1.04	1.28	38.68
2	BM-40-8	69.16	0.11	0.07	0.45	0.76	29.45
3	BM-80-8	46.13	0.79	0.04	1.5	1.24	50.3
4	BM-20-8 (clean)	93.66	0.15	0.06	0.28	0.02	5.83
5	BM-60-8 (clean)	97.69	0.02	0.00	0.36	0.00	1.93

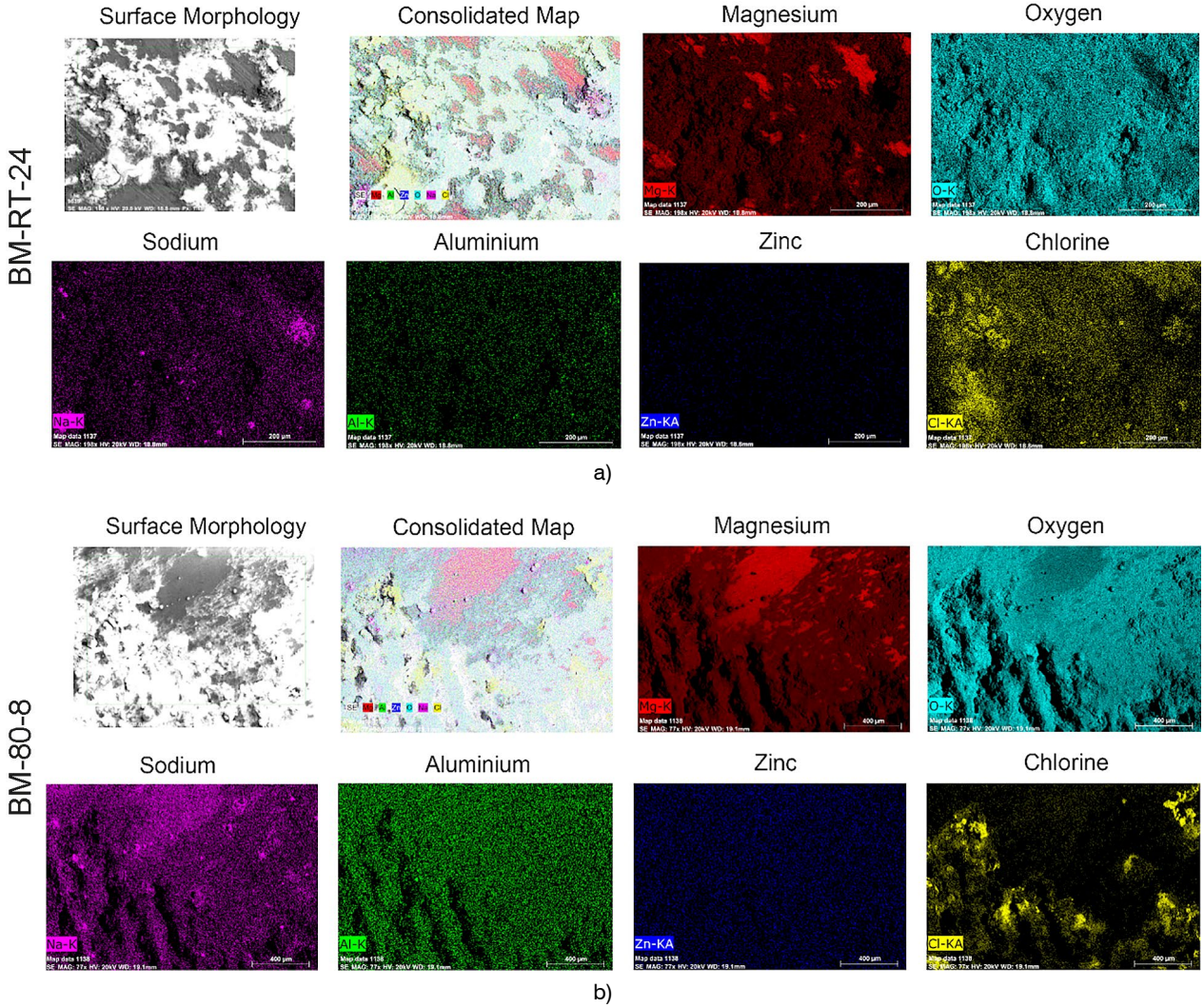

Fig. 3. Elemental map of the specimen BM-RT-24 (a) and specimen BM-80-8 (b)

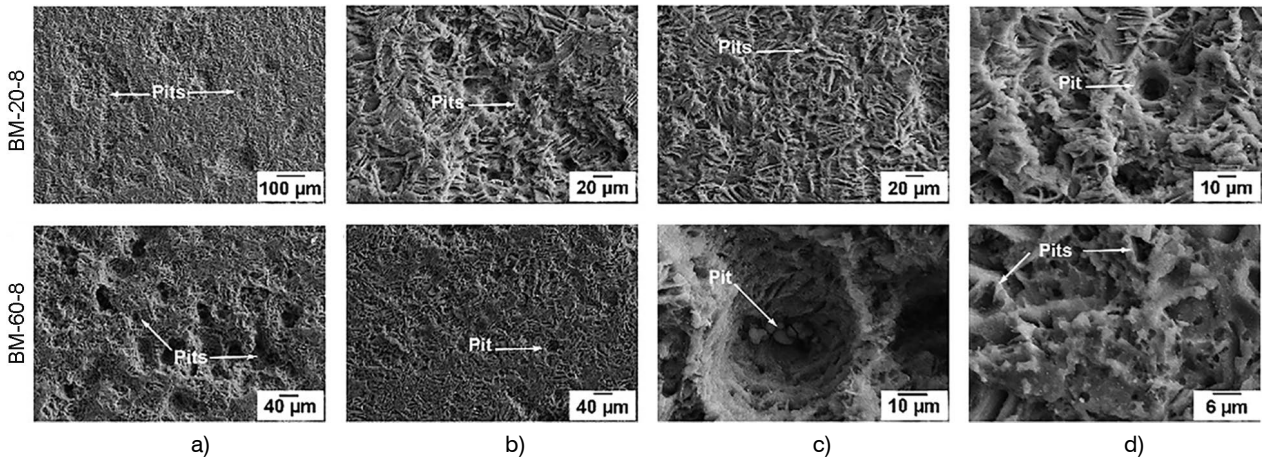

Fig. 4. Surface morphology of specimen BM-20-8 and specimen BM-60-8 after removal of corrosion products

an aluminum oxide (Al_2O_3) layer, further fortifying the protective shield. The layer acted as a formidable barrier, effectively obstructing the ingress of water and corrosive ions, thereby retarding the corrosion process. Environmental factors in seawater, including the presence of chloride ions (Cl^-), pose a formidable challenge to magnesium alloys. Chloride ions have a notorious propensity to deteriorate the protective oxide layer by

forming soluble magnesium chloride ($MgCl_2$) compounds, thereby exposing fresh metal surfaces to accelerated corrosion. Furthermore, the temperature exerted a significant influence on corrosion rates. An increase in temperatures accelerated the corrosion process, as evident in the substantial increases in corrosion rates.

Thermal-cyclic testing

The corrosion rate of the specimen subjected to thermal-cyclic testing, spanning a temperature range from –20 °C to 80 °C over a duration of 360 hours, exhibited a low value of 0.491 mm/year. The corrosion rate stands in marked contrast to the high corrosion rate obtained under

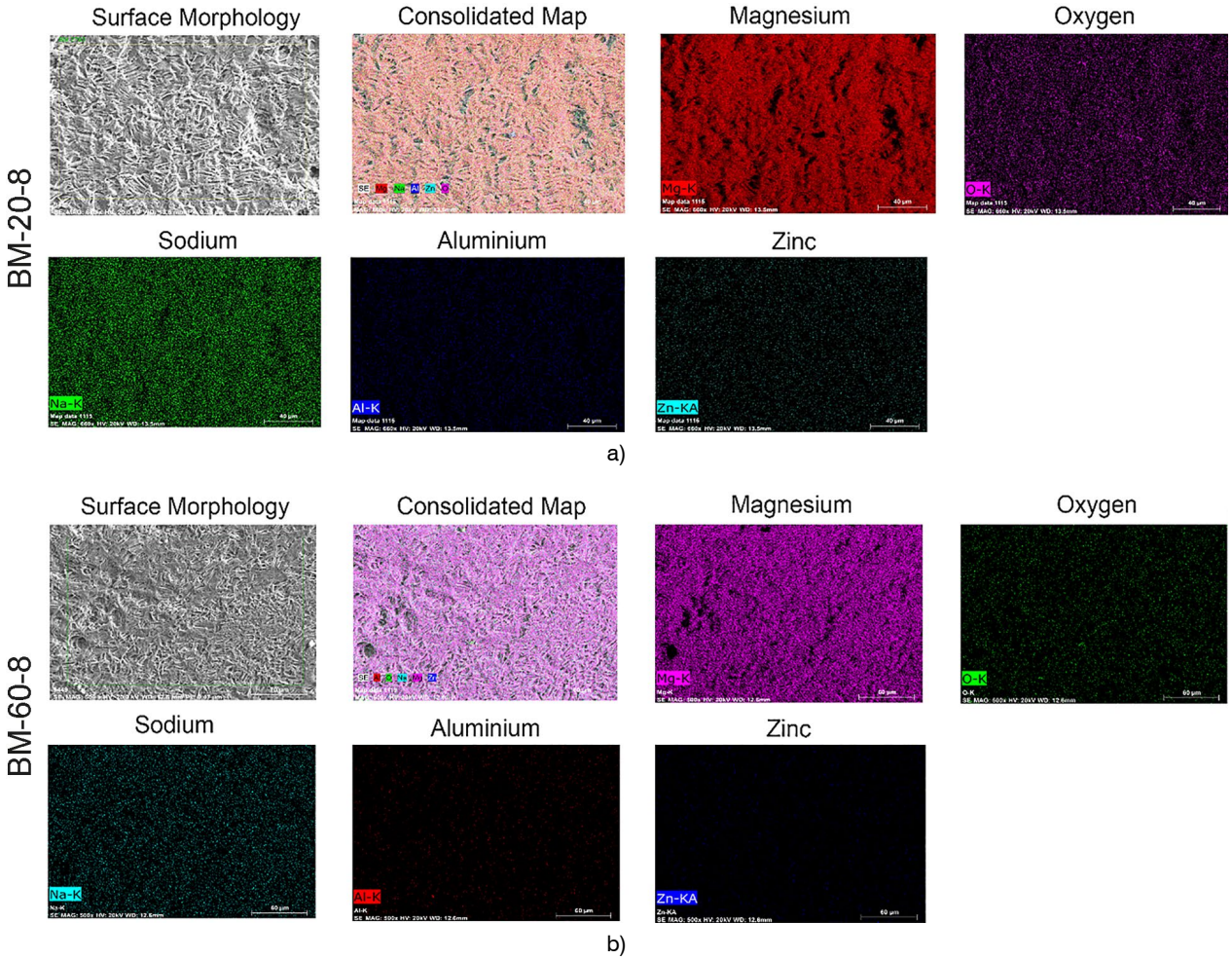

Fig. 5. Elemental map of the specimen BM-20-8 (a) and specimen BM-60-8 (b)

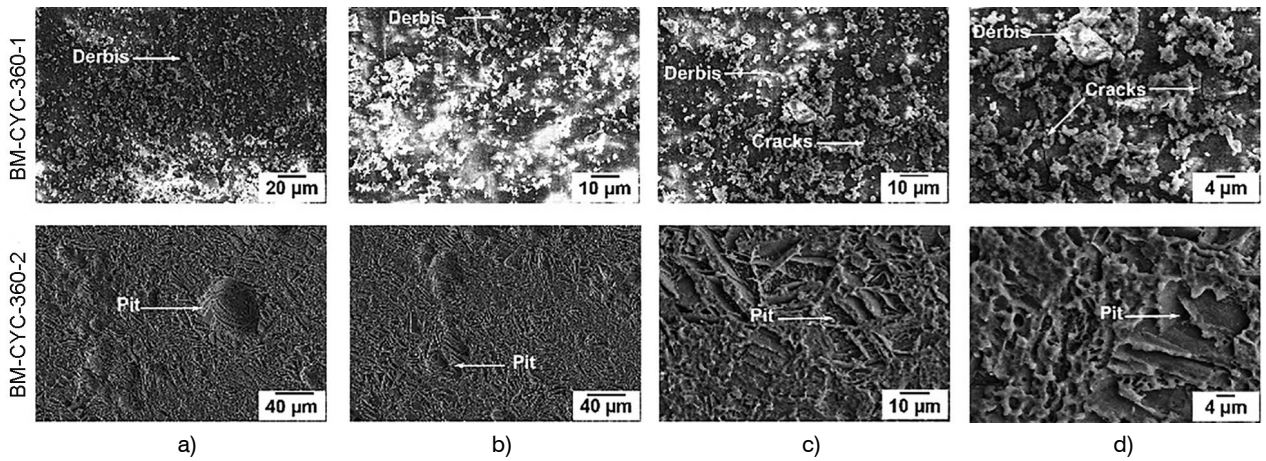

Fig. 6. Surface morphology of specimen BM-CYC-360-1 and specimen BM-CYC-360-2

thermostatic conditions. The unique phenomenon was attributed to the accumulation of debris, which included corrosion products and salts, forming a protective layer on the surface of the specimen. The protective layer effectively shielded the underlying material from undergoing further corrosion. The protective mechanism has led to the observed reduction in the corrosion rate.

In Fig. 6 the surface morphology of BM-CYC-360-1 is described. The specimen displayed cracks and corrosion debris on the surface. The reaction between hydroxide ions in the electrolyte and magnesium leads to the formation of magnesium hydroxide. Also, the debris consisted of magnesium chloride resulting from the reaction of magnesium hydroxide with chlorine. The longer immersion period likely contributed to the increased debris formation. The BM-CYC-360-2 described the surface morphology of the specimen after the removal of corrosion debris. Pits and craters were observed, with an average pit diameter of approximately 10 µm. The elemental maps in Fig. 7 confirmed that the corrosion debris predominantly consisted of $MgCl_2$. Additionally, the predominance of oxygen indicated the formation of $Mg(OH)_2$ on the surface. The corrosion mechanism was similar to that of the thermos-static corrosion process.

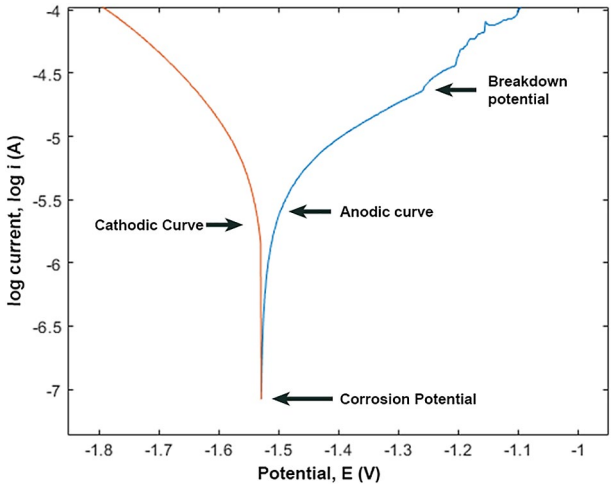

Fig. 8. Tafel plot of the specimen AZ91D

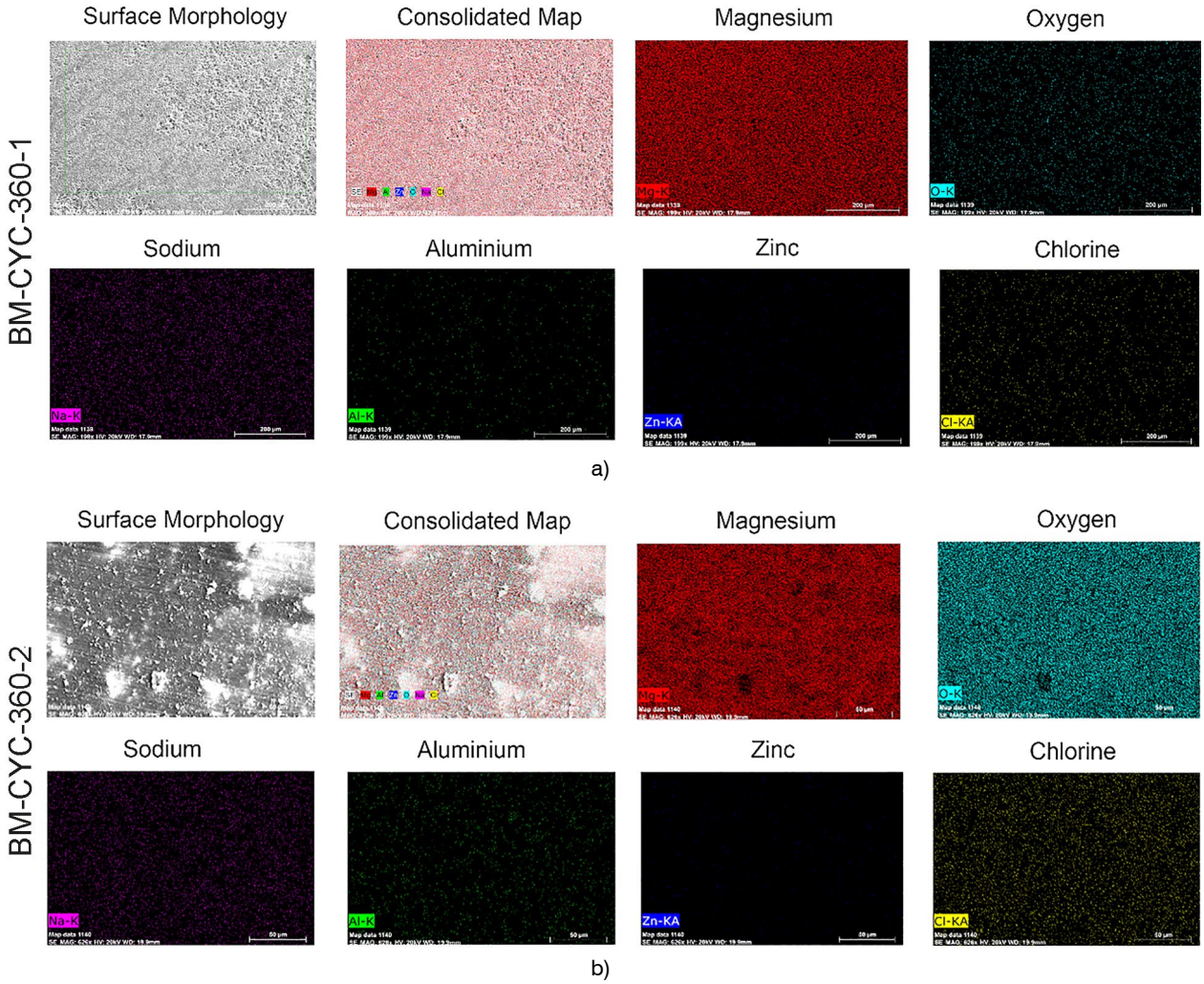

Fig. 7. Elemental map of the specimen BM-CYC-360-1 (a) and specimen BM-CYC-360-2 (b)

Electrochemical corrosion

The Tafel plot (Fig. 8), which represents the relationship between the anodic and cathodic reactions, converged at the corrosion potential of –1.576 V. Tangent lines were drawn to both the anodic and cathodic curves of the Tafel plot within 20 mV, and the corrosion current was calculated. The corrosion was computed using equation (2), resulting in a corrosion rate of 1.747 mm/year. Additionally, the specimen exhibited pitting characteristics at –1.204 V.

The change of potential over time is shown in Fig. 9. The sacrificial anode performance tests yielded an electrochemical efficiency of 750 A h/kg for AZ91D alloy. The anode consumption rate was determined to be 11.68 kg/A.yr, and the anodic efficiency was 34.1%.

CONCLUSION

The investigation into AZ91D alloy involved comprehensive analyses, encompassing microstructural examination, microhardness assessment, and thermostatic and thermocyclic testing. Advanced instrumental techniques were employed to determine surface morphology and composition. The results demonstrated the following:

- The microstructure of AZ91D alloy was characterized by the presence of primary α-Mg and a eutectic phase featuring aluminum-rich α-Mg and intermetallic β-$Mg_{17}Al_{12}$. Notably, intermetallic phases precipitated at grain boundaries, aligning with the phases identified in the Al-Mg phase diagram. The measured microhardness was 49.96 ± 1.76 HV.
- Thermostatic testing revealed a temperature-dependent increase in corrosion rate. However, thermocyclic

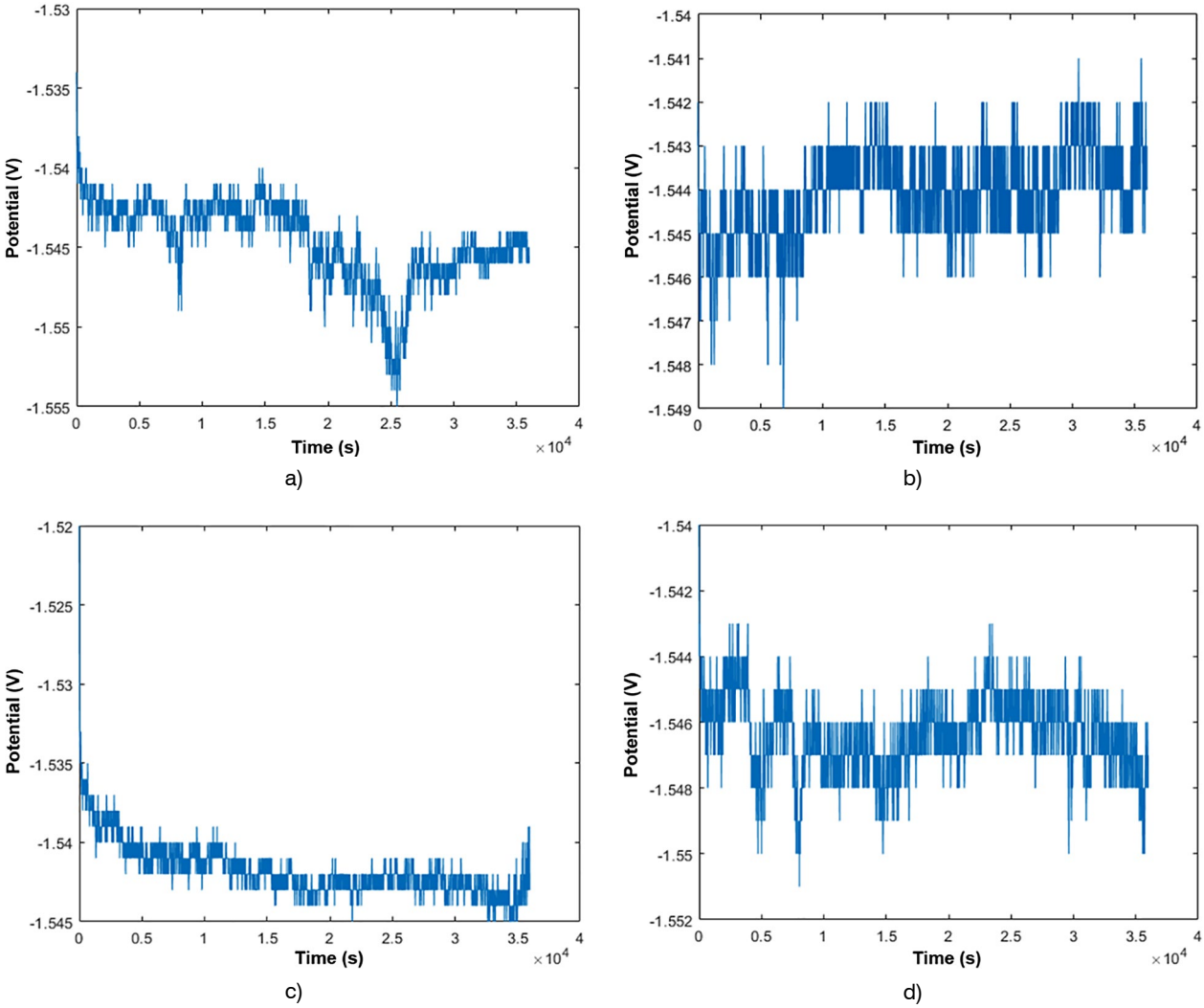

Fig. 9. Change of potential over time for the specimen at an anodic current density of: a) 15 μA.cm^{-2}; b) 4 μA.cm^{-2}; c) 40 μA.cm^{-2}; d) 15 μA.cm^{-2}

testing indicated a relatively low corrosion rate attributed to the accumulation of debris on the specimen surface.

- Electrochemical corrosion assessments demonstrated pitting corrosion initiation at -1.204 V. The alloy exhibited a sacrificial anodic performance of 37.1%, implying limited suitability for sacrificial anode applications in marine environments.

While the tested alloy demonstrated considerable performance, there is a possibility for enhancement to better suit the intended sacrificial anode application. Modifying corrosion and consumption rates through advanced techniques such as heat treatment processes, incorporating diverse alloying elements, and potentially applying specialized surface treatments hold promise in upgrading performance for optimal functionality in the marine environment.

Acknowledgement

The authors are thankful to the Science and Engineering Research Board, Department of Science and Technology, Government of India, for providing financial assistance to carry out the research work "Development of surface composites of Magnesium-Rare Earth alloy with controlled corrosion kinetics by Friction Stir Processing for sacrificial anodic applications" through the project vide "TAR/2022/000582".

Conflicts of interest

The authors declare no conflict of interest or competing interests for the research work.

Availability of data and material (data transparency)

All data generated or analyzed during this study are included in this published article (and its supplementary information files).

REFERENCE

1. Gudze, M.; Melchers, R., Operational based corrosion analysis in naval ships. *Corrosion science* **2008,** *50* (12), 3296-3307.
2. Jinglei, Z.; Keliang, S.; Xiuming, H.; Jiande, Y.; Shujie, P., Cathodic protection of A1 hull ship. *Chinese Journal of Oceanology and Limnology* **1990,** *8*, 257-262.
3. Seymour, A. J., Cathodic protection for corrosion control of ships and other steel structures in seawater. *Anti-Corrosion Methods and Materials* **1990**.
4. Xu, L.; Xin, Y.; Ma, L.; Zhang, H.; Lin, Z.; Li, X., Challenges and solutions of cathodic protection for marine ships. *Corrosion Communications* **2021,** *2*, 33-40.
5. Bellezze, T.; Fratesi, R.; Roventi, G., Cathodic protection of a ship propeller shaftby impressed current anodes. *La Metallurgia Italiana* **2014**.
6. Botha, C., Cathodic protection for ships. *Marine Technology* **2000**, 31-35.
7. Bulatović, S.; Aleksić, V.; Zečević, B., Corrosion protection of ship structures Zaštita od korozije brodskih konstrukcija. *PROCEEDINGS KNJIGA RADOVA* **2021**, 177.
8. Hossen, A.; Mahmud, R.; Islam, A., Minimization of corrosion in aquatic environment – a review. *Int J Hydro* **2023,** *7* (1), 9-16.
9. Nazari, M. H.; Zhang, Y.; Mahmoodi, A.; Xu, G.; Yu, J.; Wu, J.; Shi, X., Nanocomposite organic coatings for corrosion protection of metals: A review of recent advances. *Progress in Organic Coatings* **2022,** *162*, 106573.
10. Thomas, D.; Philip, E.; Sindhu, R.; Ulaeto, S. B.; Pugazhendhi, A.; Awasthi, M. K., Developments in smart organic coatings for anticorrosion applications: a review. *Biomass Conversion and Biorefinery* **2022,** *12* (10), 4683-4699.
11. Govindaraju, M.; Vignesh, R. V.; Padmanaban, R., Effect of heat treatment on the microstructure and mechanical properties of the friction stir processed AZ91D magnesium alloy. *Metal Science and Heat Treatment* **2019,** *61* (5-6), 311-317.
12. Gusieva, K.; Davies, C.; Scully, J.; Birbilis, N., Corrosion of magnesium alloys: the role of alloying. *International Materials Reviews* **2015,** *60* (3), 169-194.
13. Balan, P.; Thiagarajan, V.; Ganesan, S. P.; Raghunathan, V.; Shankar, K. V.; Kumar, B. Y.; Ramalingam, V. V., Characterization of powder metallurgy processed magnesium alloys for biomedical implants. *Emergent Materials* **2023,** *6* (2), 573-581.
14. Li, H.; Paidar, M.; Ojo, O. O.; Vignesh, R. V.; Iswandi, I.; Mehrez, S.; Zain, A. M.; Mohanavel, V., Effect of tool profile on wear and mechanical behaviors of CeO_2 and ZrO_2-reinforced hybrid magnesium matrix composite developed via FSP technique. *Journal of Manufacturing Processes* **2023,** *94*, 297-315.
15. Paidar, M.; Bokov, D.; Mehrez, S.; Ojo, O. O.; Ramalingam, V. V.; Memon, S., Improvement of mechanical and wear behavior by the development of a new tool for the friction stir processing of Mg/B_4C composite. *Surface and Coatings Technology* **2021,** *426*, 127797.
16. Meifeng, H.; Lei, L.; Yating, W.; Zhixin, T.; Wenbin, H., Corrosion properties of surface-modified AZ91D magnesium alloy. *Corrosion science* **2008,** *50* (12), 3267-3273.
17. Candan, S.; Unal, M.; Turkmen, M.; Koc, E.; Turen, Y.; Candan, E., Improvement of mechanical and corrosion properties of magnesium alloy by lead addition. *Materials Science and Engineering: A* **2009,** *501* (1-2), 115-118.
18. Ezhilselvi, V.; Nithin, J.; Balaraju, J.; Subramanian, S., The influence of current density on the morphology and corrosion properties of MAO coatings on AZ31B magnesium alloy. *Surface and Coatings Technology* **2016,** *288*, 221-229.
19. Liang, J.; Hu, L.; Hao, J., Improvement of corrosion properties of microarc oxidation coating on magnesium alloy by optimizing current density parameters. *Applied Surface Science* **2007,** *253* (16), 6939-6945.
20. Razzaghi, M.; Mirzadeh, H.; Emamy, M., Mechanical properties of Mg–Al–Mn magnesium alloys with low Al content in the as-cast and extruded conditions. *Materials Research Express* **2019,** *6* (10), 106521.

21. Reza Kashyzadeh, K.; Amiri, N.; Maleki, E.; Unal, O., A Critical Review on Improving the Fatigue Life and Corrosion Properties of Magnesium Alloys via the Technique of Adding Different Elements. *Journal of Marine Science and Engineering* **2023,** *11* (3), 527.
22. Yao, C.; Wang, Z.; Tay, S. L.; Zhu, T.; Gao, W., Effects of Mg on microstructure and corrosion properties of Zn–Mg alloy. *Journal of Alloys and Compounds* **2014,** *602*, 101-107.
23. Ramalingam, V. V.; Ramasamy, P.; Kovukkal, M. D.; Myilsamy, G., Research and development in magnesium alloys for industrial and biomedical applications: a review. *Metals and Materials International* **2020,** *26*, 409-430.
24. Vaira Vignesh, R.; Padmanaban, R.; Govindaraju, M.; Suganya Priyadharshini, G., Investigations on the corrosion behaviour and biocompatibility of magnesium alloy surface composites AZ91D-ZrO_2 fabricated by friction stir processing. *Transactions of the IMF* **2019,** *97* (5), 261-270.
25. Vignesh, R. V.; Padmanaban, R.; Govindaraju, M., Investigations on the surface topography, corrosion behavior, and biocompatibility of friction stir processed magnesium alloy AZ91D. *Surface Topography: Metrology and Properties* **2019,** *7* (2), 025020.
26. Vignesh, R. V.; Padmanaban, R.; Govindaraju, M.; Priyadharshini, G. S., Mechanical properties and corrosion behaviour of AZ91D-HAP surface composites fabricated by friction stir processing. *Materials Research Express* **2019,** *6* (8), 085401.
27. Loto, C. A.; Loto, R. T.; Popoola, A. P., Cathodic protection performance evaluation of magnesium anodes on mild steel corrosion in 0.5MH_2SO_4 and seawater environments. *Journal of Bio-and Tribo-Corrosion* **2019,** *5*, 1-7.
28. Azzeddine, H.; Hanna, A.; Dakhouche, A.; Rabahi, L.; Scharnagl, N.; Dopita, M.; Brisset, F.; Helbert, A.-L.; Baudin, T., Impact of rare-earth elements on the corrosion performance of binary magnesium alloys. *Journal of Alloys and Compounds* **2020,** *829*, 154569.
29. Sanmiguel-May, J. A.; López-Alcantara, R.; Juárez-Arellano, E. A.; Pérez-Quiroz, J. T.; Contreras, A.; Pérez-López, T., Performance Assessment of Magnesium Anodes Manufactured by Sintering Process. *Metals* **2021,** *11* (3), 406.
30. Zidane, N.; Albrimi, Y. A.; Addi, A. A.; Douch, J.; Souto, R.; Hamdani, M., Evaluation of the corrosion of AZ31 magnesium alloy used as sacrificial anode for cathodic protection of hot-water tank storage containing chloride. *Int. J. Electrochem. Sci* **2018,** *13*, 29-44.
31. Rzychoń, T.; Michalska, J.; Kiełbus, A., Corrosion resistance of Mg-RE-Zr alloys. *Journal of Achievements in Materials and Manufacturing Engineering* **2007,** *21* (1), 51-54.
32. Yasakau, K.; Bastos, A.; Haffner, D.; Quandt, E.; Feyerabend, F.; Ferreira, M.; Zheludkevich, M., Sacrificial protection of Mg-based resorbable implant alloy by magnetron sputtered Mg5Gd alloy coating: A short-term study. *Corrosion Science* **2021,** *189*, 109590.
33. Umoru, L.; Ige, O., Effects of tin on aluminum–zinc–magnesium alloy as sacrificial anode in seawater. *Journal of Minerals & Materials Characterization & Engineering* **2007,** *7* (2), 105-113.
34. Quevedo, M.; Genesca, J., Influence of turbulent flow on the corrosion of Al–Zn–Mg galvanic anode in artificial seawater media. *Materials and corrosion* **2009,** *60* (6), 424-430.
35. Robinson, H.; George, P., Effect of alloying and impurity elements in magnesium alloy cast anodes. *Corrosion* **1954,** *10* (6), 182-188.
36. Sun, H.; Liu, L.; Li, Y.; Ma, L.; Yan, Y., The performance of Al–Zn–In–Mg–Ti sacrificial anode in simulated deep water environment. *Corrosion science* **2013,** *77*, 77-87.
37. Abubakar, M.; Onimisi, M. A., Effect of Precipitation Hardening Treatment on Corrosion Behavior and Anodic Efficiency of Sacrificial Anode Produced from Recycled Al–Zn–Mg Alloy. *Journal of Failure Analysis and Prevention* **2021,** *21* (4), 1212-1219.
38. Pathak, S. S.; Mendon, S. K.; Blanton, M. D.; Rawlins, J. W., Magnesium-based sacrificial anode cathodic protection coatings (Mg-rich primers) for aluminum alloys. *Metals* **2012,** *2* (3), 353-376.
39. Sekar, P.; Sanna, N.; Desai, V., Enhancement of resistance to galvanic corrosion of ZE41 Mg alloy by equal channel angular pressing. *Materials and Corrosion* **2020,** *71* (4), 571-584.
40. Kajánek, D.; Hadzima, B.; Buhagiar, J.; Wasserbauer, J.; Jacková, M., Corrosion degradation of AZ31 magnesium alloy coated by plasma electrolytic oxidation. *Transportation Research Procedia* **2019,** *40*, 51-58.
41. Muazu, A.; Aliyu, Y. S.; Abdulwahab, M.; Idowu Popoola, A. P., Sacrificial anode stability and polarization potential variation in a ternary Al–*x*Zn–*x*Mg alloy in a seawater-marine environment. *Journal of Marine Science and Application* **2016,** *15*, 208-213.
42. Radhika, K.; Lakshminarayanan, A., An insight into the stress corrosion cracking resistance of friction stir processed and micro arc oxidation coated ZE41 grade magnesium alloy. *Proceedings of the Institution of Mechanical Engineers, Part C: Journal of Mechanical Engineering Science* **2022,** *236* (2), 1255-1273.
43. Ling, M.; Mehrez, S.; Vignesh, R. V.; Zain, A. M.; Paidar, M.; Kharche, N. A.; Mohanavel, V., Investigation on underwater friction stir processing of AZ-61 magnesium alloy. *Materials Today Communications* **2023,** *36*, 106885.
44. Raj, V.; Sabarinath, S.; Ramalingam, V. V., Biodegradable Magnesium Alloy-Based Composites: Properties, Processing, and Surface Coatings – A Review. *Transactions of the Indian Institute of Metals* **2023**, 1-9.
45. Song, G. L.; Atrens, A., Corrosion mechanisms of magnesium alloys. *Advanced engineering materials* **1999,** *1* (1), 11-33.